Icarus 415 (2024) 116078

Contents lists available at ScienceDirect

Icarus

journal homepage: www.elsevier.com/locate/icarus

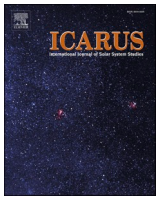

Synthetic analogs for lava flows on the surface of Mercury: A mid-infrared study

Andreas Morlok [a,*], Alexander Sehlke [b], Aleksandra N. Stojic [a], Alan Whittington [c], Iris Weber [a], Maximilian P. Reitze [a], Harald Hiesinger [a], Jörn Helbert [d]

[a] Institut für Planetologie, Wilhelmstr.10, 48149 Münster, Germany
[b] NASA Ames Research Center, Moffett Field, CA 94035, USA
[c] Department of Earth and Planetary Sciences, The University of Texas at San Antonio, USA
[d] Institute for Planetary Research, DLR, Rutherfordstrasse 2, 12489 Berlin, Germany

ARTICLE INFO

Keywords:
Mercury (planet)
Space probes
Infrared spectroscopy
Regolith

ABSTRACT

We studied a series of hermean lava analogs in the mid-infrared (2.5 μm–18 μm) to provide characteristic spectra for enstatite basalt, the Northern Volcanic Plains and Na-rich Northern Volcanic Plains. Our aim is to provide spectra for the interpretation of the data expected from Mercury from the MERTIS (MErcury Radiometer and Thermal Infrared Spectrometer) instrument on the ESA/JAXA BepiColombo mission.

Bulk powder spectra show bands of glass with a dominating broad Si-O-Si stretching feature around 10 μm. Crystalline components are mainly enstatite and forsterite with Reststrahlen Bands (RBs) around 9.3 μm, 9.6–9.9 μm, 10.0 μm, and 10.3–10.7 μm. Increasing intensity of crystalline features in the spectra reflect the increase in the crystallites in glass with decreasing temperature of equilibration and quenching. Micro-FTIR data allowed to extract spectral of individual components and glass. The position of the Christiansen Feature (CF) has only a weak correlation with the degree of crystallinity.

Correlations are observed between the Christiansen Feature (CF) and the bulk SiO_2 content of the materials, as does the correlation of this feature with the compositional index SCFM = $SiO_2/(SiO_2 + CaO + FeO + MgO)$ on an atomic basis. This study also confirms the correlation line of glass-rich, irradiated Mercury analogs in these systems (Weber et al.,2023), indicating a similar spectral response of the glass rich materials expected for the surface of Mercury. The position of the strongest silicate main band (MB) compared to the SiO_2 content, confirms a trend for samples formed in experiments simulating high velocity impacts fall on a different trend line than analog samples formed in magmatic processes.

A comparison of the results to an Earth-based hermean surface spectrum showed similarities to spectra obtained for NVP samples.

1. Introduction

The ongoing ESA/JAXA mission to Mercury, BepiColombo, will allow investigation of the hermean surface in detail (Grard and Balogh, 2001). An important part of the scientific payload is the mid-infrared (MIR) spectrometer MERTIS (MErcury Radiometer and Thermal Infrared Spectrometer) that will help to assess the surface mineralogy of the planetary crust and to provide the petrographic context simultaneously (Hiesinger et al., 2010, 2020). MERTIS will obtain spectra in the MIR range from orbit and map the planet in a spatial resolution of 500 m in the wavelength range of 7 μm to 14 μm (Hiesinger et al., 2010, 2020). The MIR shows a multitude of spectral features of alumina-silicate based rock-forming minerals, which will enable MERTIS to 'decipher' Mercury's surface mineralogy (e.g., Rothery et al., 2020).

For the interpretation of the data that are expected after the hermean orbit is reached in 2025, a spectral database is needed that is comprised of natural rock forming minerals, but also of analogue minerals and rocks that represent the unique weathering conditions on Mercury (e.g., Weber et al., 2023). These weathering conditions have great potential to modify the initial petrographic assemblage and its associated spectral properties. Two facilities, the IRIS laboratory in Münster and the BED laboratory in Berlin were established to investigate natural and

* Corresponding author.
E-mail address: morlokan@uni-muenster.de (A. Morlok).

https://doi.org/10.1016/j.icarus.2024.116078
Received 5 January 2024; Received in revised form 2 April 2024; Accepted 3 April 2024
Available online 8 April 2024

synthetic samples relevant to Mercury (Maturilli et al., 2008; Weber et al., 2018).

Since there are no unambiguously identified meteorites from Mercury (e.g., Weber et al., 2016), we have to rely on remote sensing data, experiments, and modelling to estimate sample compositions of interest for the MIR analyses. Based on such studies using the data from the NASA MESSENGER missions X-ray, gamma-ray, and neutron spectrometers (e.g., Peplowski et al., 2015; Peplowski and Stockstill-Cahill, 2019; Nittler et al., 2020), major element ratios were obtained. This allowed the identification of regions with characteristic chemical composition, the geochemical terranes, with a derived mineralogy similar to that of terrestrial komatiites, boninites, and andesites (Nittler et al., 2011; Peplowski et al., 2015; Peplowski and Stockstill-Cahill, 2019; Weider et al., 2015; Vander Kaaden and McCubbin, 2016). On the basis of this data, modelling, and laboratory experiments indicated a mineral assemblage dominated by iron-poor olivine and pyroxene, as well as plagioclase, with minor quartz (e.g., Charlier et al., 2013; Stockstill-Cahill et al., 2012; Sehlke and Whittington, 2015; Namur and Charlier, 2017; Vander Kaaden and McCubbin, 2016; Renggli et al., 2022).

MIR spectroscopy of Mercury has been limited to date, owing to difficult terrestrial telescopic observation conditions (e.g., Schulz and Benkhoff, 2006). These studies of large surface regions indicate a composition dominated by plagioclase and pyroxene (Sprague et al., 1994, 2000, 2002, 2007; Sprague and Roush, 1998; Emery et al., 1998; Cooper et al., 2001).

Infrared laboratory studies for the BepiColombo mission so far covered natural samples in the form of terrestrial impact rocks (Morlok et al., 2016a, 2016b); minerals of interest, like feldspars (Reitze et al., 2020, 2021, 2022, 2023), meteorites (Weber et al., 2016; Morlok et al., 2017a, 2020a), and lunar samples (Morlok et al., 2022). Synthetic analogs were based on laboratory experiments of crustal formation processes by Namur and Charlier (2017), and Morlok et al. (2017b, 2019, 2021, 2023). Points of interest were processes affecting hermean rocks, like hypervelocity impacts (Morlok et al., 2020b) and space weathering (Weber et al., 2020, 2021, 2023; Stojic et al., 2021, 2023).

One of the findings of the MESSENGER mission was the identification of extensive large-scale volcanic structures (e.g., Thomas et al., 2015). Sehlke and Whittington (2015) experimentally studied the evolution of rheological properties (e.g., viscosity) of three basaltic compositions analog to Mercury's surface, based on findings from the MESSENGER data. Namely, an enstatite basalt, and two magnesium basalts were investigated as compositional end-members comprising the Northern Volcanic Plains (NVP) (Fig. 1). The results suggest that the formation of the extensive smooth lava plains of Mercury could be due to large effusion rates (flood basalts) and not to unusually fluid lavas.

The aim of this study is to obtain MIR reflectance spectra for the lava flows on young Mercury using the synthetic analogues from Sehlke and Whittington (2015). This crucial addition will fill a chemical composition and structural gap in the mineral and rock spectral database. Identifying spectral features that can help to identify volcanic and impact structures (i.e., here specifically by impact melt) based on spectroscopic features is of particular interest. The glass component can be expected to make up a substantial part of the hermean surface materials because it forms not only by rapid cooling of volcanic melts but also during large- and small-scale impacts onto the surface. The latter is an important process on Mercury, as the impact flux is suggested to be more than five times higher and the impactors have a much higher velocity than on the Moon, where glasses are already important constitutes of the regolith (Cintala, 1992).

2. Materials and methods

2.1. Sample synthesis and characterization

Three series of materials with magnesium-rich basalt compositions were synthesized. Two were based on the Northern Volcanic Plains compositions with low (NVP) and high Na_2O (NVPNa) variants (0.2 wt% and 6.2 wt% Na_2O). The third is an enstatite-rich (ENBAS) basalt derived from a partial melt produced from the Indarch EH4 chondrite (McCoy et al., 1999). A detailed description of the sample synthesis is given in Sehlke and Whittington (2015).

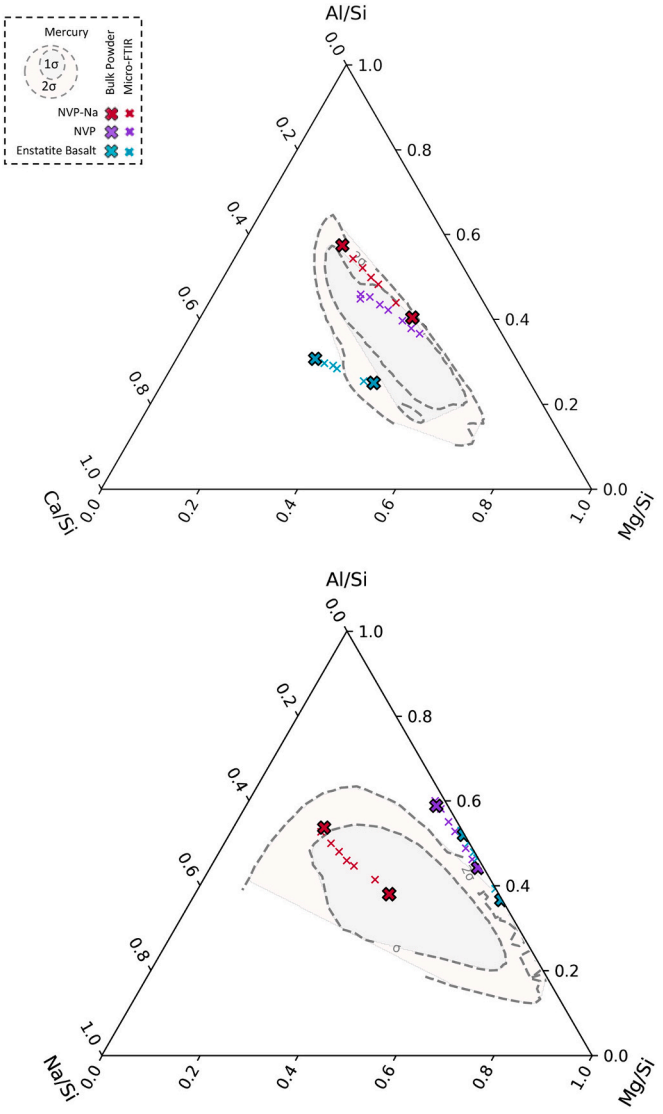

Fig. 1. Overview of the chemical composition of the studied samples (wt%, from Sehlke and Whittington, 2015). Grey contours [R1–2] are compositional space from earlier Mercury analog studies (Outer dashed line: 2 sigma, inner dashed line: 1 sigma). Sources: Morlok et al. (2017a, 2017b, 2019, 2021, 2023), Large crosses are compositions of bulk samples, small crosses these of glass materials.

Decarbonated oxide and carbonate mixtures were heated in a muffle furnace up to 1600 °C. Quenching was achieved by pouring the melt onto a copper plate. For each starting composition, samples were quenched at a series of temperatures ranging from 1378 °C to 1200 °C. Based on the composition of the residual melt at the lowest quenching temperature of each series, the bulk chemical composition of the 'evolved' samples was derived (Table 1a and b). For each run product, the chemical compositions were analysed using EMPA and the glass/crystallites ratio was determined (Sehlke and Whittington, 2015). For details of the quenching temperatures and chemical compositions see Table 1a and b. Fig. 1 gives an overview of the major elements in the starting composition, as well as the composition of the glass fraction in

Table 1
(a) Quench temperatures, ID numbers and and glass contents of the samples used in this study (from Sehlke and Whittington, 2015). (b) Chemical composition of the analysed bulk and glass phases (from Sehlke and Whittington, 2015). In wt%, From Sehlke and Whittington (2015). B = Bulk composition, M = in-situ analysis. Glass: Fraction of glass to crystalline components. Also see Fig. 1.

a)

Enstatite Basalt (ENBAS)	Quench Temp.	ID	#Glass
Glass	1363°	ID 395	1.00
Evolved	1249°	ID 396	1.00
	1303°	ID 397	0.97
	1287°	ID 407	0.89
	1273°	ID 408	0.84
	1257°	ID 409	0.80
	1249°	ID 410	0.78
	1238°	ID 398	0.58
Northern Volcanic Plains (NVP)			
Glass	1324°	ID 403	1.00
Evolved	1228°	ID 414	1.00
	1317°	ID 404	0.95
	1304°	ID 411	0.92
	1286°	ID 412	0.84
	1266°	ID 405	0.81
	1245°	ID 413	0.77
	1228°	ID 406	0.58
Northern Volcanic Plains, Na-rich (NVPNa)			
Glass	1378°	ID 399	1.00
Evolved	1200°	ID 438	1.00
	1342°	ID 400	0.98
	1322°	ID 424	0.93
	1301°	ID 425	0.90
	1281°	ID 402	0.84
	1260°	ID 426	0.81
	1240°	ID 427	0.77
	1200°	ID 401	0.71

b)

Enstatite Basalt		GLASS	SCFM	SiO_2	TiO_2	Al_2O_3	Cr_2O_3	FeO	MnO	MgO	CaO	Na_2O	K_2O	P_2O_5
ID 395 (Glass)	B	1.00	0.63	55.06	0.18	13.07	0.00	0.29	0.14	19.72	12.37	0.04	0.08	0.04
ID 396 (Evolved)	B	1.00	0.66	54.80	0.26	15.41	0.03	0.26	0.05	12.42	15.27	0.04	0.08	0.05
ID 397	B	0.97	0.63	55.06	0.18	13.07	0.00	0.29	0.14	19.72	12.37	0.04	0.08	0.04
ID 407	B	0.89	0.63	55.06	0.18	13.07	0.00	0.29	0.14	19.72	12.37	0.04	0.08	0.04
ID 408	B	0.84	0.63	55.06	0.18	13.07	0.00	0.29	0.14	19.72	12.37	0.04	0.08	0.04
ID 409	B	0.80	0.63	55.06	0.18	13.07	0.00	0.29	0.14	19.72	12.37	0.04	0.08	0.04
ID 410	B	0.78	0.63	55.06	0.18	13.07	0.00	0.29	0.14	19.72	12.37	0.04	0.08	0.04
ID 398	B	0.58	0.63	55.06	0.18	13.07	0.00	0.29	0.14	19.72	12.37	0.04	0.08	0.04
ID 395 (Glass)	M	1.00	0.63	55.06	0.18	13.07	0.00	0.29	0.14	19.72	12.37	0.04	0.08	0.04
ID 407	M	1.00	0.66	56.19	0.20	15.00	0.00	0.33	0.14	14.25	14.06	0.04	0.10	0.07
ID 409	M	1.00	0.66	54.86	0.21	16.15	0.01	0.35	0.13	12.52	15.42	0.04	0.10	0.06
ID 398	M	1.00	0.67	56.86	0.23	15.66	0.03	0.31	0.14	12.21	14.95	0.05	0.10	0.06
Northern Volcanic Plains														
ID 403 (Glass)	B	1.00	0.69	57.10	0.96	15.27	0.67	3.61	0.25	16.53	4.95	0.29	0.31	0.05
ID 414 (Evolved)	B	1.00	0.75	58.63	1.28	17.40	0.20	2.62	0.07	10.06	6.88	0.49	0.45	0.07
ID 404	B	0.95	0.69	57.10	0.96	15.27	0.67	3.61	0.25	16.53	4.95	0.29	0.31	0.05
ID 411	B	0.92	0.69	57.10	0.96	15.27	0.67	3.61	0.25	16.53	4.95	0.29	0.31	0.05
ID 412	B	0.84	0.69	57.10	0.96	15.27	0.67	3.61	0.25	16.53	4.95	0.29	0.31	0.05
ID 405	B	0.81	0.69	57.10	0.96	15.27	0.67	3.61	0.25	16.53	4.95	0.29	0.31	0.05
ID 413	B	0.77	0.69	57.10	0.96	15.27	0.67	3.61	0.25	16.53	4.95	0.29	0.31	0.05
ID 406	B	0.58	0.69	57.10	0.96	15.27	0.67	3.61	0.25	16.53	4.95	0.29	0.31	0.05
ID 403 (Glass)	M	1.00	0.69	57.10	0.96	15.27	0.67	3.61	0.25	16.53	4.95	0.29	0.31	0.05
ID 414 (Evolved)	M	1.00	0.75	58.63	1.28	17.40	0.20	2.62	0.07	10.06	6.88	0.49	0.45	0.07
ID 411	M	1.00	0.71	56.99	1.05	16.05	0.09	3.66	0.24	14.35	5.41	0.32	0.35	0.05
ID 413	M	1.00	0.74	58.68	1.21	17.84	0.03	3.66	0.26	10.80	6.39	0.40	0.41	0.06
ID 406	M	1.00	0.74	59.17	1.25	17.85	0.06	3.74	0.23	9.90	6.72	0.44	0.43	0.07
ID 399 (Glass)	B	1.00	0.73	55.02	0.89	14.88	0.18	2.88	0.25	13.59	4.29	6.25	0.22	0.01
ID 438 (Evolved)	B	1.00	0.81	59.00	1.12	19.25	0.02	2.67	0.11	5.81	5.34	7.13	0.27	0.01

(*continued on next page*)

Table 1 (*continued*)

b)

Enstatite Basalt		GLASS	SCFM	SiO_2	TiO_2	Al_2O_3	Cr_2O_3	FeO	MnO	MgO	CaO	Na_2O	K_2O	P_2O_5
ID 400	B	0.98	0.73	55.02	0.89	14.88	0.18	2.88	0.25	13.59	4.29	6.25	0.22	0.01
ID 424	B	0.93	0.73	55.02	0.89	14.88	0.18	2.88	0.25	13.59	4.29	6.25	0.22	0.01
ID 425	B	0.90	0.73	55.02	0.89	14.88	0.18	2.88	0.25	13.59	4.29	6.25	0.22	0.01
ID 402	B	0.84	0.73	55.02	0.89	14.88	0.18	2.88	0.25	13.59	4.29	6.25	0.22	0.01
ID 426	B	0.81	0.73	55.02	0.89	14.88	0.18	2.88	0.25	13.59	4.29	6.25	0.22	0.01
ID 427	B	0.77	0.73	55.02	0.89	14.88	0.18	2.88	0.25	13.59	4.29	6.25	0.22	0.01
ID 401	B	0.71	0.73	55.02	0.89	14.88	0.18	2.88	0.25	13.59	4.29	6.25	0.22	0.01
ID 399 (Glass)	M	1.00	0.73	55.02	0.89	14.88	0.18	2.88	0.25	13.59	4.29	6.25	0.22	0.01
ID 424	M	1.00	0.76	57.01	0.95	16.08	0.09	2.86	0.25	10.75	4.58	6.31	0.23	0.01
ID 402	M	1.00	0.78	56.37	0.99	16.67	0.06	2.98	0.23	8.57	4.80	7.00	0.24	0.01
ID 427	M	1.00	0.80	57.59	1.03	17.50	0.04	3.04	0.23	6.65	4.98	7.05	0.25	0.01
ID 401	M	1.00	0.81	57.89	1.07	18.00	0.01	3.03	0.22	5.49	5.12	7.04	0.26	0.01

the specific samples in comparison to the analogue samples for Mercury used in earlier studies (Sehlke and Whittington, 2015).

The mineralogy of the ENBAS samples is dominated by enstatite and forsterite, of NVP by spinel and enstatite, and of NVPNa by spinel and forsterite. The mineral phases are embedded in a matrix of silicate glass.

Formation of feldspar was inhibited by quenching above the temperature at which it joins the crystallization sequence, which is just below 1200 °C (Sehlke and Whittington, 2015).

2.2. Infrared studies

In order to produce different size fractions, bulk sample material was crushed in a steel mortar. The resulting powder was cleaned using acetone and dry sieved using an automatic Retsch Tap Sieve into four size fractions: <25 μm, 25 μm to 63 μm, 63 μm to 125 μm, and 125 μm to 250 μm.

2.2.1. Bulk powder studies

For the bi-directional reflectance analyses of the size fractions, we filled aluminium cups (1 cm diameter and flattened the surface with a spatula following Mustard and Hays (1997). For the bulk powder analyses we used a Bruker Vertex 70v infrared system at the IRIS laboratory in Münster.

Analyses were made in MIR from 2.5 μm to 18 μm. To ensure a high signal to noise ratio (SNR), a cooled liquid N_2 MCT detector was applied. For each spectrum, 512 scans were made under low pressure (10^{-3} bar) at room temperature. The background was removed by ratioing against a diffuse gold standard (INFRAGOLD™) measured under identical conditions. For various optical geometries, analyses presented here were made with a variable geometry stage (Bruker A513) at 20° incidence (i) and 30° emergence angle (e). While the spectral range of the MERTIS spectrometer is 7 μm to 14 μm, features at shorter and longer wavelengths are also of general interest. Therefore, and for better visibility, we present powder spectra from 7 μm to 18 μm (Fig. 2, Table 2).

Important features in the spectra are the characteristic emission high or reflectance low, the Christiansen Feature (CF). This feature marks a region of low scattering, of sudden increase of the absorption coefficient next to the point where the index of refraction is near unity (King et al., 2004). The CF is usually easily identified in remote sensing spectra, and is correlated to the chemical bulk composition, and thus used as proxy for the bulk composition (e.g. Cooper et al., 2002). The Transparency Feature (TF) is typical for the powdered fine grain size fraction (<25°μm and thus important as an indicator for lower grain sizes. Here, volume scattering increases by small grain size together with increasing porosity (Salisbury and Wald, 1992; Mustard and Hays, 1997). The Reststrahlen Bands (RBs) are the vibrational modes of the molecular groups and thus the actual spectral 'fingerprint'. They are strongest among the larger grain sizes owing to a larger surface area supporting more reflection. We refer to the strongest feature among the RBs as the Main Band (MB) (King et al., 2004).

The planetary remote sensing data expected from Mercury will be dominated by emission. For the transformation of reflectance into emission Kirchhoff's law is applied: Emission = 1 − Reflectance (e.g. Nicodemus, 1965). An important condition is that Kirchhoffs law requires the reflected light being collected in all directions. This is best done by using a gold coated hemisphere. In this work, we applied a bi-directional, variable mirror setup. This is needed since we are interested in the effects of varying incidence and exit angles expected from the orbital observation geometries of the orbiter. The differences in the setups affect relative reflectance intensities and spectral contrast, while band shape and positions remain comparable (Salisbury et al., 1991; Hapke, 1993; Thomson and Salisbury, 1993; Salisbury et al., 1994; Christensen et al., 2001; King et al., 2004).

The spectra presented in this study are available at the IRIS database of the Institut für Planetologie in Münster (http://bc-mertis-pl.uni-muenster.de).

2.2.2. Micro-FTIR

All specular reflectance spectra were acquired in the wavelength range between 2.8 μm and 12.5 μm with a dry air purged Hyperion 3000 μ-FTIR microscope attached to the Bruker Vertex 80v in the IRIS lab at the Institut für Planetologie at the University of Münster.

The surfaces of all polished embedded grains were investigated with a cooled liquid N_2 64 × 64-pixel focal plane array (FPA) detector, recording 4096 pixels during each scan simultaneously. In order to improve the SNR each measurement was integrated over 64 scans. We did not bin the spectra, resulting in a spatial resolution of 2.7 × 2.7 μm^2/pixel.

The spectra were measured against an internal polished gold standard. In the micro-FTIR studies all analyses were made on polished blocks, thus a TF does not occur in these analyses (Reitze et al., 2023). Each resulting hyperspectral block (4096 pixels) was factorized and the spectra were simultaneously normalized to the maximum and minimum intensities (0 and 1) to identify spectrally distinct areas. Between 20 and 30 single spectra were extracted and averaged from each region of interest (ROI). If not stated otherwise, all spectra were smoothed following the Savitzky Golay method using 20 points smoothing window. Finally, the average spectrum of the entire hyperspectral block (4096 pixels) was derived for each aliquot (denoted as average hyperspectral block), these spectra represent a mixed spectrum of the previously identified spectrally distinct areas in each aliquot.

Representative scans of areas in three selected samples are presented in Fig. 3. Phases identified in the hyperspectral block are color-coded, the resulting summary spectra are presented in the same color in the figures. Band positions are presented in Table 2.

Since Micro-FTIR spectra are obtained from polished samples, they cannot exhibit the TF of the finest grain size fractions. They are essentially similar to the larger grain size fractions of the powdered materials.

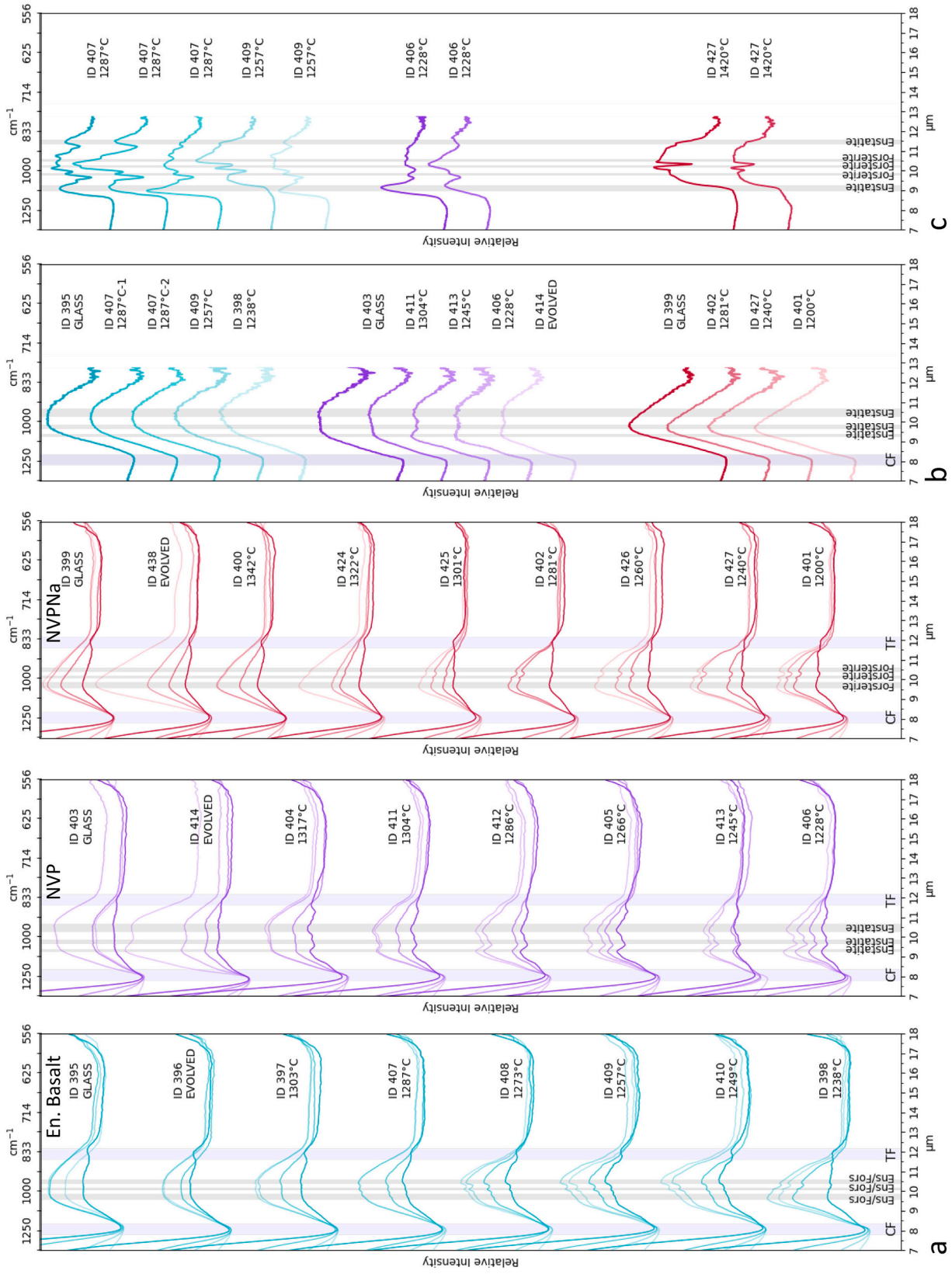

Fig. 2. Mid-infrared spectra (in µm) (a) Bulk spectra of powdered size fractions. Color saturation increases from coarsest (125–250 µm) to finest (<25 µm) size fraction. Ens/Fors = Overlapping Enstatite/Forsterite features. Sample with high glass content are on top, with increasing crystallinity toward bottom spectrum/sample. The temperatures given are quenching temperatures in sample synthesis. (b) Micro-FTIR spectra of glass extracted from hyperspectral data. (c) Micro-FTIR spectra of representative crystalline phases extracted from hyperspectral data block. Vertical shaded areas: blue are CF (left) and TF (right), grey mark ranges of band positions in this study for RBs characteristic for specific minerals. Reference: Hofmeister (1987, 1997)), Hamilton (2000, 2010), Lane et al. (2011), Stojic et al. (2021). (For interpretation of the references to color in this figure legend, the reader is referred to the web version of this article.)

Table 2
Overview of the band positions for bulk and micro-FTIR analyses (in μm). (a) Enstatite Basalts, (b) Northern Volcanic Plains (NVP) and (c) Na-rich Northern Volcanic Plains (NVPNa). Also see Figs. 2 and 3.

a)

BULK		CF					TF		
ID 395	0–25 μm	8.16		9.94	10.55		12.04		
(Glass)	25–63 μm	8.15		10.05					
	63–125 μm	8.16		10.02					
	125–250 μm	8.16		9.94					
ID 396	0–25 μm	8.06		10.50			11.89		
(Evolved)	25–63 μm	8.08		10.31					
	63–125 μm	8.06		10.07				14.39	
	125–250 μm	8.04		10.13					
ID 397	0–25 μm	8.09		10.11	10.57		11.98		
	25–63 μm	8.09		9.96	10.59				
	63–125 μm	8.05		10.11	10.47				
	125–250 μm	8.06		10.13	10.43				
ID 407	0–25 μm	8.06			10.52		11.98		
	25–63 μm	8.11	9.92	10.13	10.55				
	63–125 μm	8.04	9.88	10.13	10.45				
	125–250 μm	8.00		10.13	10.45				
ID 408	0–25 μm	8.12		10.13	10.55		11.98		
	25–63 μm	8.13	9.90	10.13	10.52				
	63–125 μm	8.08		10.13	10.47			15.91	
	125–250 μm	8.04		10.13	10.47				
ID 409	0–25 μm	8.13		10.13	10.55		12.01		
	25–63 μm	8.13		10.13	10.47				
	63–125 μm	8.05		10.13	10.47			14.43	
	125–250 μm	8.04	9.59	10.13	10.50			15.64	
ID 410	0–25 μm	8.16		10.11	10.62		12.01		
	25–63 μm	8.11		10.13	10.45				
	63–125 μm	8.08		10.13	10.50			15.54	
	125–250 μm	8.05		10.13	10.52				
ID 398	0–25 μm	8.04	9.75		10.47	11.37	11.92		
	25–63 μm	8.04	9.69	10.09	10.47				
	63–125 μm	8.02	9.67	10.11	10.43				
	125–250 μm	7.95	9.65	10.11	10.45				
MICRO-FTIR									
Glass									
ID 395		8.14		10.19					
ID 407 (1)		8.05		10.18					
ID 407 (2)		8.07		10.18					
ID 409		7.95			10.47				
ID 398		8.10			10.56				
Crystal									
ID 407		8.09	9.13		9.88	10.16	10.44	10.78	11.49
ID 407		8.40	9.22		9.87	10.39			11.55
ID 407		8.08	9.03		9.88	10.34		10.80	11.36
ID 409		8.22		9.66		10.16	10.53		11.41
ID 409		8.16	9.02	9.56	9.87	10.19		10.80	11.47

b)

BULK		CF					TF	
ID 403	0–25 μm	8.00		9.71	10.69	11.89	14.70	15.43
(Glass)	25–63 μm	7.98		9.67	10.57			
	63–125 μm	7.98			10.59			
	125–250 μm	8.00		9.71	10.57		14.85	
ID 414	0–25 μm	7.89	9.38		10.52	10.84		

(continued on next page)

Table 2 (*continued*)

b)

BULK		CF					TF	
(Evolved)	25–63 μm	7.86	9.36		10.64			15.18
	63–125 μm	7.87	9.36		10.59		13.28	
	125–250 μm	7.82	9.36		10.57			
ID 404	0–25 μm	8.02	9.32	9.94	10.40	11.68		15.49
	25–63 μm	7.97	9.36	9.90	10.45			
	63–125 μm	8.00		9.94	10.38			
	125–250 μm	7.94		9.92	10.45			
ID 411	0–25 μm	8.02	9.34		10.43	11.68		
	25–63 μm	7.98	9.34		10.43			
	63–125 μm	7.94	9.30	9.88	10.31		14.80	
	125–250 μm	7.93	9.36		10.36		14.57	
ID 412	0–25 μm	8.11	9.27		10.36	11.74		
	25–63 μm	8.02	9.32		10.38			
	63–125 μm	7.95	9.32		10.31			15.23
	125–250 μm	7.89	9.30		10.34		14.66	
ID 405	0–25 μm	8.02	9.30		10.43	11.60		
	25–63 μm	7.97	9.30		10.36			
	63–125 μm	7.95	9.30	9.90	10.36			
	125–250 μm	7.93	9.30		10.34			
ID 413	0–25 μm	8.09	9.30		10.55	11.71	14.43	
	25–63 μm	8.02	9.30	9.88	10.38	11.68	14.34	
	63–125 μm	7.97	9.32	9.90	10.38		14.34	15.69
	125–250 μm	7.93	9.32	9.85	10.36		14.39	15.33
ID 406	0–25 μm	7.98	9.32		10.50	11.83	14.39	
	25–63 μm	7.97	9.27	9.88	10.43		14.34	
	63–125 μm	7.91	9.30	9.88	10.38		14.34	
	125–250 μm	7.89	9.27	9.85	10.40		14.43	15.28
MICRO-FTIR								
Glass								
ID 403		7.82				10.53		
ID 411		7.85				10.38		
ID 413		8.01		9.30	9.86	10.40		
ID 406		7.85		9.39		10.37		
ID 414		7.72		9.46		10.54		
Crystal								
ID 406		7.84	9.16		9.80	10.50	10.80	
ID 406		8.00	9.27			10.38		11.71

c)

BULK		CF			TF		
ID 399	0–25 μm	8.08	9.75		11.98		15.54
(Glass)	25–63 μm	8.05	9.73				
	63–125 μm	8.09	9.73				
	125–250 μm	8.02	9.85				
ID 438	0–25 μm	8.12	9.81		11.92	14.43	15.04
(Evolved)	25–63 μm	8.08	9.79				
	63–125 μm	8.04	9.75				
	125–250 μm	8.01	9.79				
ID 400	0–25 μm	8.02	9.77		11.92		
	25–63 μm	8.05	9.71				15.09
	63–125 μm	8.01	9.69				
	125–250 μm	8.04	9.71				15.75
ID 424	0–25 μm	8.13	9.77	10.52	12.01		
	25–63 μm	8.11	9.71	10.43			

(*continued on next page*)

Table 2 (*continued*)

c)									
BULK		CF					TF		
	63–125 μm	8.06	9.75		10.43				15.75
	125–250 μm	8.02	9.73						
ID 425	0–25 μm	8.09	9.73		10.62	11.37	11.92		15.23
	25–63 μm	8.09	9.69	10.11	10.47			13.96	
	63–125 μm	8.06	9.71	10.11	10.45			14.04	15.64
	125–250 μm	7.98	9.67	10.09	10.45				
ID 402	0–25 μm	8.05	9.79		10.57	11.37	11.92		
	25–63 μm	8.06	9.67	10.11	10.47			13.91	15.54
	63–125 μm	8.01	9.71	10.09	10.45				
	125–250 μm	8.02	9.73	10.09	10.45				
ID 426	0–25 μm	8.11	9.71		10.50		11.95	14.21	15.18
	25–63 μm	8.05	9.71	10.11	10.52			14.85	15.64
	63–125 μm	8.05	9.67	10.13	10.50			14.04	
	125–250 μm	8.01	9.65	10.11	10.47			14.00	15.69
ID 427	0–25 μm	8.12	9.67		10.59	11.31	11.68		15.54
	25–63 μm	8.06	9.63	10.11	10.52			14.39	15.69
	63–125 μm	8.01	9.61	10.11	10.47				15.91
	125–250 μm	8.04	9.63	10.11	10.45			14.34	15.54
ID 401	0–25 μm	8.06	9.69		10.59	11.26			
	25–63 μm	8.04	9.69	10.11	10.47				15.75
	63–125 μm	7.94	9.65	10.11	10.45			14.34	
	125–250 μm	7.95	9.65	10.11	10.47			13.91	
MICRO-FTIR									
Glass									
ID 399		8.00	9.82						
ID 402		8.02	9.73						
ID 427		8.02	9.80						
ID 401		7.98	9.74						
Crystal									
ID 427		8.12				10.21	10.49		
ID 427		8.12			9.92	10.18		10.79	

This has to be kept in mind in the use of Micro-FTIR spectra for direct comparisons with remote sensing data.

Similar to the bi-directional set-up used for the bulk studies, the Micro-FTIR optics cannot completely related to emission via Kirchhoff's Law. This again affects spectral contrast, while band positions and band shapes remain comparable (Salisbury and Wald, 1992; Moersch and Christensen, 1995; Mustard and Hays, 1997).

2.3. Data processing and presentation

For the processing of the chemical and spectral data, peak finding, and presentation we used the Pyrolite Python open-source packages (Williams et al., 2020), Pandas (McKinney, 2010), Numpy (Harris et al., 2020), Matplotlib (Hunter, 2007), Seaborn (Waskom, 2021), and SciPy (Virtanen et al., 2020).

3. Results

3.1. Enstatite Basalts (EB) (Figs. 2, 3) (Table 2a)

Among the bulk spectra (Fig. 2a), the two samples consisting entirely of glass, (ID 395 and ID 396), have spectral features typical for amorphous materials: a single, dominating RB between 9.9 μm to 10.1 μm for ID 395 and from 10.1 μm to 10.5 μm for ID396. In the latter case, the broad shape of the glass feature makes an exact location of the band difficult to define. The CF for ID 395 is at 8.2 μm, for ID 396 between 8.0 μm- and 8.1 μm, the TFs are at 12.0 μm and 11.9 μm, respectively.

With increasing degree of crystallization, several sharper forsterite and enstatite RBs appear (Hofmeister, 1987, 1997; Hamilton, 2000, 2010; Lane et al., 2011): ID 397 shows an RB between 10.0 μm and 10.1 μm, which occurs in all following spectra. Similarly, a feature between 10.4 μm and 10.6 μm occurs, which is also observed in most of the spectra. An additional RB is seen between 9.6 μm and 9.9 μm in ID398, ID 407, ID 408, and ID 409.

The CF location remains rather constant (8.0 μm to 8.2 μm) among the increasingly crystalline aliquots and is similar to the glass-rich aliquots. Also, the TF is located between 11.9 μm and 12.0 μm. Minor features are observed at wavelengths longer than 15 μm, which can be attributed to a bending mode of olivine beyond the second CF (Lane et al., 2011).

The general shape of the spectra also changes, the RB are just minor features on top of a broad, amorphous band. With increasing crystallinity for most samples, the 10.4 μm to 10.6 μm RB becomes the strongest feature. In the crystal-rich end-member ID 398 the feature between 9.7 μm and 9.8 μm turns out to be strongest.

The extracted glass spectra from the micro-FTIR scans (Fig. 2b; 3a and b) show a uniform behaviour: a CF from 8.0 μm–8.1 μm) and a broad MB typical for amorphous material that ranges between 10.2 μm and 10.6 μm.

Micro-FTIR analyses of typical crystalline inclusions (Fig. 2c; 3a and b) exhibit enstatite and forsterite features:

Features in ID 407 and ID 409 from 9.0 μm–9.2 μm, 9.6 μm–9.9 μm,

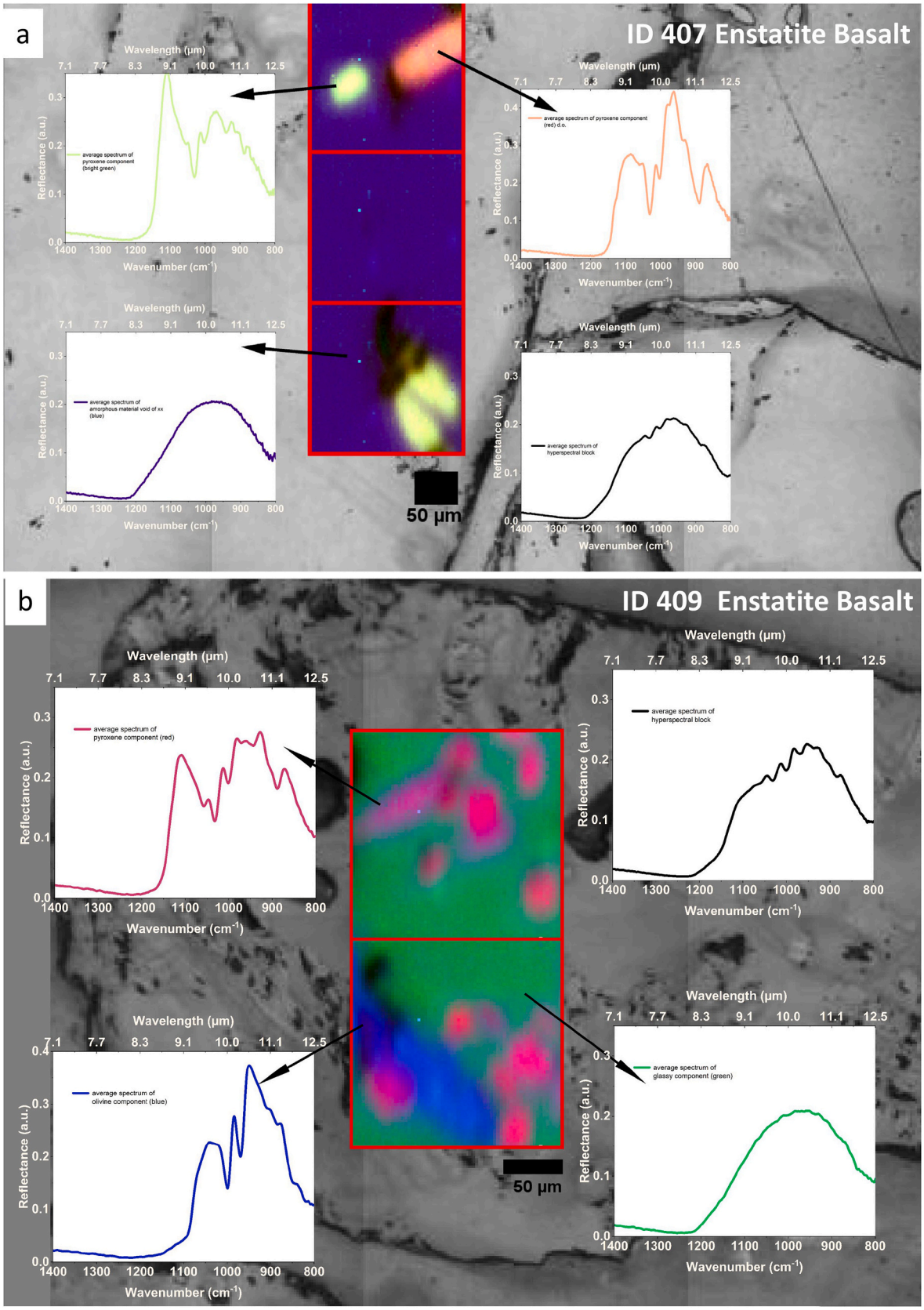

Fig. 3. Representative areas of micro-FTIR studies using the high-resolution FPA detector. Color-coded areas are phases extracted from the hyperspectral block. Details see Fig. 2 and Table 2.

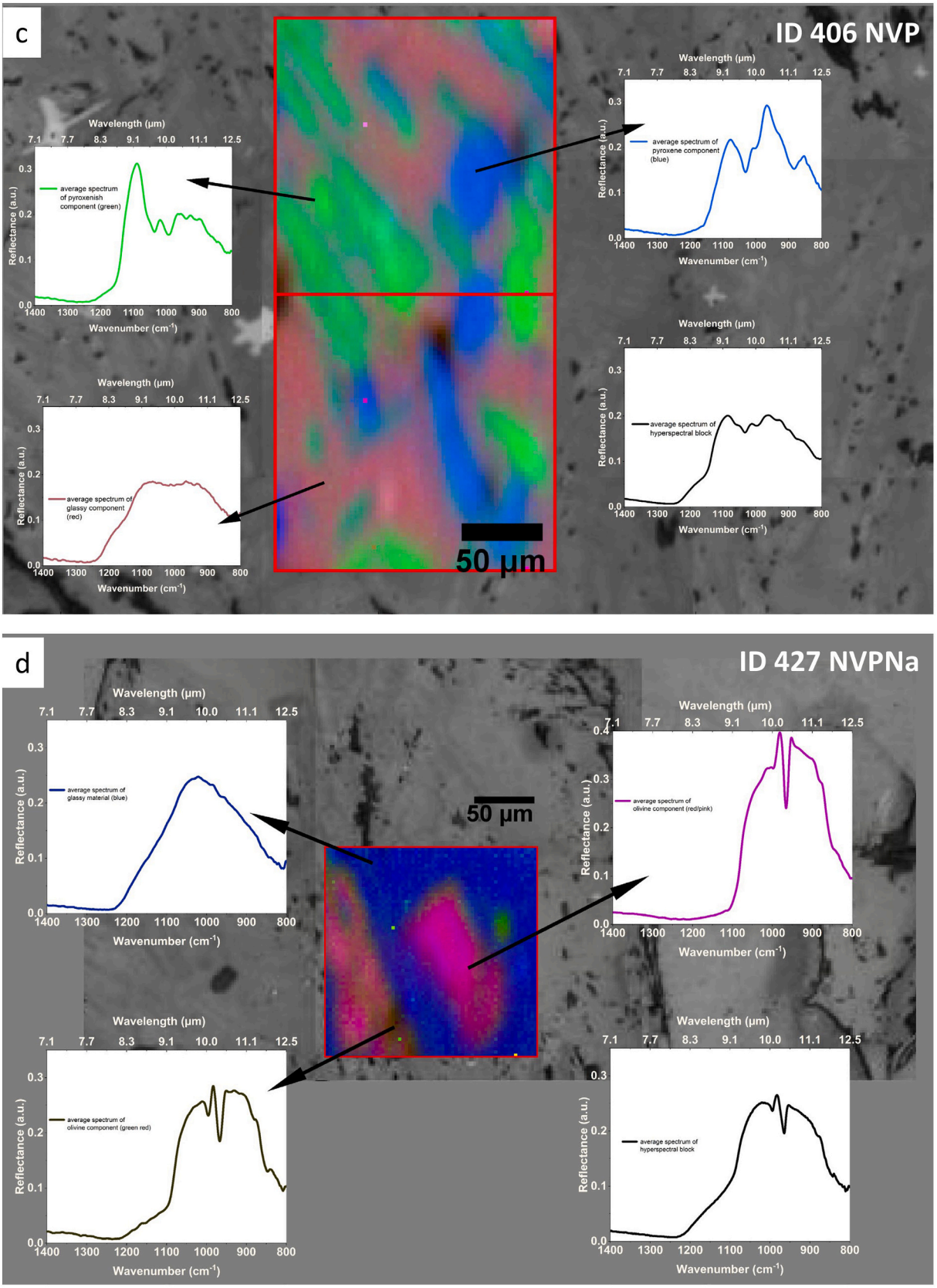

Fig. 3. (*continued*).

10.2 μm–10.5 μm, and 11.4 μm–11.6 μm overlap with both enstatites and forsterites, (e.g., Hofmeister, 1987, 1997; Hamilton, 2000, 2010; Lane et al., 2011; Stojic et al., 2021). Differences in band shapes and band positions are due to the variances in crystal orientation.

3.2. Northern Volcanic Plains (NVP) (Figs. 2, 3) (Table 2b)

For the spectra of bulk samples (Fig. 2a), the glass-rich endmember ID 403 has a dominating RB between 10.6 μm and 10.7 μm, and a

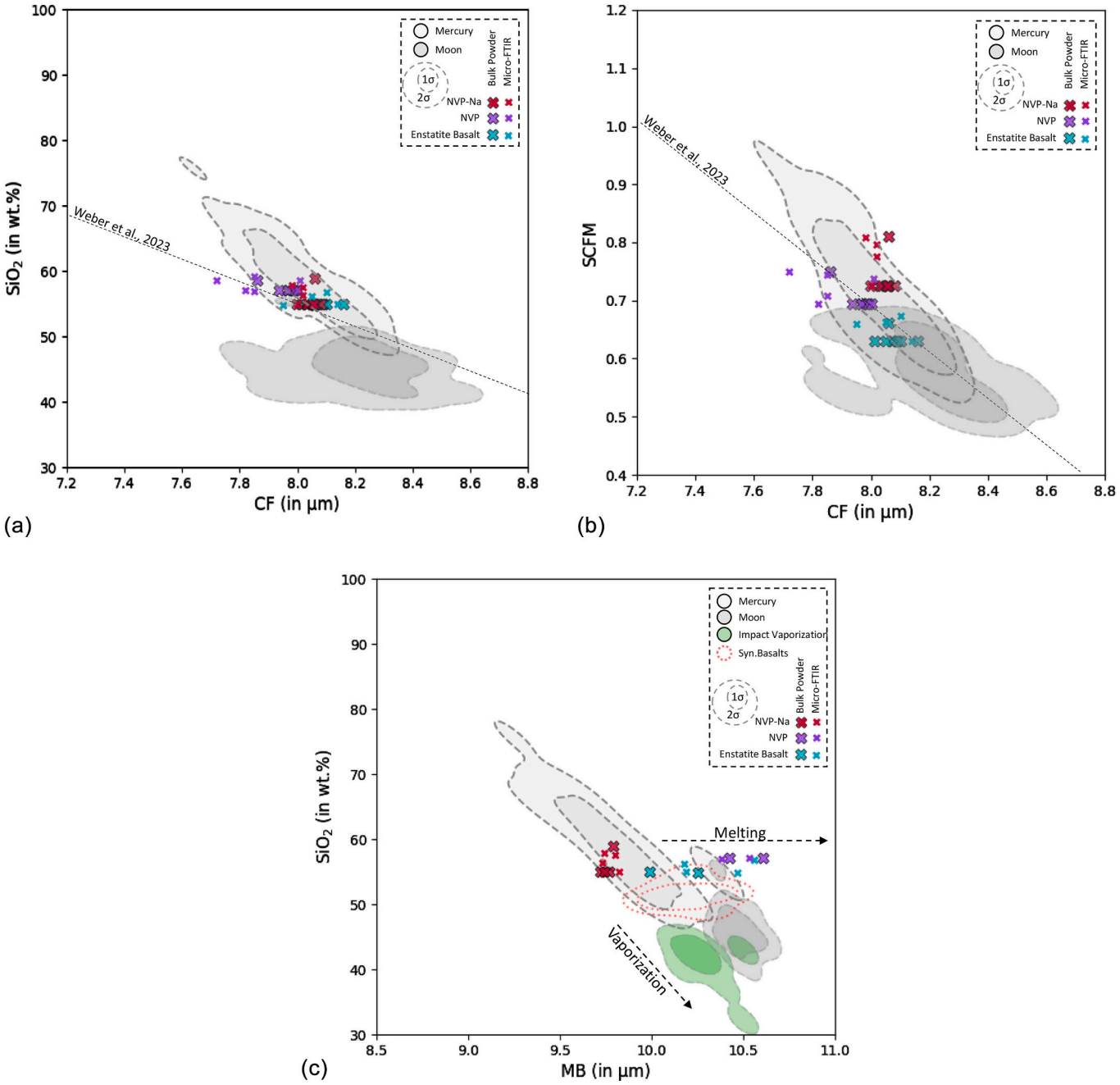

Fig. 4. Shaded areas: outer dashed line: 2 sigma, inner dashed line: 1 sigma of the data (a) Comparison of the CF (in μm) with the SiO2 content (in wt%). The CF is a proxy for the bulk composition of the observed material (e.g. Cooper et al., 2002). The micro-FTIR analyses plot above the bulk spectra due to their slightly different composition. They also plot along the correlation line for irradiated analog materials (Weber et al., 2023), which represent agglutinates of crystalline and glassy materials. Lunar reference sources: Allen et al. (2012) Donaldson Hanna et al. (2017), Morlok et al. (2019, 2022), Salisbury et al. (1997), Zeng et al. (2019). Mercury reference sources: Morlok et al. (2017a, 2017b, 2019, 2021, 2023).
(b) Comparison of the CF to the SCFM index (SiO_2/SiO_2 + CaO + FeO + MgO) (Salisbury and Walter, 1989), a proxy for the polymerization of a material. Results from this study plot along the correlation line for irradiated analog materials (Weber et al., 2023), which represent agglutinates of crystalline and glassy materials), a tendency observed in earlier studies. Micro-FTIR samples tend to plot above the bulk samples, result of their higher glass content. Lunar reference sources: Allen et al. (2012) Donaldson Hanna et al. (2017), Morlok et al. (2019, 2022), Zeng et al. (2019). Mercury reference sources: Morlok et al. (2017a, 2017b, 2019, 2021, 2023).
(c) Comparison of the single, dominating RB in glassy spectra (MB) with the SiO_2 content. A linear correlation for SiO_2 contents >55 wt% possibly splits into a horizontal trend for magmatic processes such as synthetic basaltic glasses (Dufresne et al., 2009), and a continuing trend for materials formed in high velocity impact/vaporization processes. Lunar reference sources: Morlok et al. (2022), Zeng et al. (2019). Mercury reference sources: Morlok et al. (2017a, 2017b, 2019, 2021). Impact vaporization experiments reference sources: Morlok et al. (2016a, b, 2020a, 2020b). Synthetic basalt glass reference sources: Dufresne et al. (2009).

shoulder/minor feature at 9.7 μm. The CF (8.0 μm) is similar to the entire range of samples of this group (ID 403, ID 414, ID 404, ID 411, ID 412, ID 405, ID 413, and ID 406), which is between 7.8 μm and 8.1 μm. Similar, in the finest grain size fraction, the TF is in a narrow range from 11.6 μm to 11.9 μm.

Emerging RBs with increasing crystallinity were identified as two strong enstatite features at 9.3 μm–9.4 μm and 10.3 μm–10.7 μm, and a weaker one at 9.7 μm–9.9 μm. At longer wavelengths, minor features are observed at 14.3 μm −14.9 μm, and 15.2 μm–15.7 μm.

The NVP micro-FTIR glass spectra (ID 403, ID 411, ID 413, ID 406, ID 414) (Fig. 2b; 3c) show more features than those from the enstatite basalts: the CF ranges from 7.7 μm to 8.0 μm, but only the ID 403 and ID 411 spectra have entirely glassy spectra with a broad RB at 10.5 μm and 10.4 μm, respectively. In-situ spectra from ID 413, ID 406, and ID 414 exhibit several RBs between 9.3 μm–9.5 μm, 9.9 μm, and 10.4 μm–10.5 μm. This can be explained by the high abundance of crystallites, which make 'pure' glass analyses difficult.

Micro-FTIR analyses of crystallites (Fig. 2c; 3c) show the typical enstatites for ID 406, probably in two different orientations with strong enstatite features at 9.2–9.3 μm, 10.4–10.5 μm (Hamilton, 2000). However, bands at 9.8 μm and 10.8 μm are also indicative of forsterite (Hofmeister, 1987, 1997; Hamilton, 2010; Lane et al., 2011). Spinels, which have been observed via EMPA (Sehlke and Whittington, 2015) turned out too small to be resolved by micro-FTIR.

3.3. Northern Volcanic Plains, Na-rich (NVPNa) (Figs. 2, 3) (Table 2c)

Bulk powder spectra of the NVPNa samples (ID 399, ID 438, ID 400, ID 424, ID 425, ID 402, ID 426, ID 427 and ID 401) (Fig. 2a) show that the CF falls into a narrow range of 7.9 μm to 8.1 μm. The TF is found between 11.3 μm and 12 μm. Among the samples having crystallites, the glass-rich ID 400 exhibits no recognizable RBs. Beginning with ID 424 NVPNa with 7% crystalline phases (Sehlke and Whittington, 2015), we see the forsterite bands at 9.6 μm–9.9 μm dominating in all spectra of samples in this group, additional RBs at 10.1 μm and 10.4 μm–10.6 μm. Weaker RBs are found at longer wavelengths between 13.9 μm to 14.6 μm and 15 μm–15.9 μm.

The micro-FTIR studies of glass (ID 399, ID 402, ID 427 and ID 401) (Fig. 2b; 3d) show again a uniform picture: the CF is at 8 μm, the broad RB between 9.7 μm and 9.8 μm. Analyses of crystallites (Fig. 2c; 3d) have typical forsterite bands in ID 427 with RBs at, 10.2 μm, 10.5 μm, and 10.8 μm (Hofmeister, 1987, 1997).

4. Discussion

4.1. CF vs. SiO_2 (Fig. 4a)

The CF as a reflectance minimum (or emission maximum) is a spectral feature easily identified even in data with a low SNR. The CF position is material constant and can be correlated with the ratio of mafic cations vs. silica content, it is therefore a convenient proxy that can be used to classify the bulk composition of the observed material according to its SiO_2 content (e.g., Cooper et al., 2002). The results for the bulk analyses in this study fall into the intermediate region, and exhibit only a small variation in the CF position (Fig. 4a). The micro-FTIR analyses plot slightly offset in relation to the bulk spectra as expected due to their different composition. The results of this study also fall along the correlation line for partly laser irradiated [R1–1] hermean analog material (Weber et al., 2023) and also confirm earlier studies (e.g. Cooper et al., 2002). These are agglutinates of crystalline and glassy materials, indicating a similar spectral behaviour of the glass-rich materials expected for the surface of Mercury.

4.2. CF vs. SCFM (Fig. 4b)

A method to link the CF to the degree of polymerization of the material is the SCFM index ($SiO_2/SiO_2 + CaO + FeO + MgO$) (Salisbury and Walter, 1989; Cooper et al., 2002). Also, these results (Fig. 4b) fall along the correlation line for partly irradiated analog samples (Weber et al., 2023), a tendency observed for many glass-rich samples confirming the coherent spectral behaviour of the expected glass rich hermean surface materials (Morlok et al., 2017b, 2019, 2021, 2022). Micro-FTIR samples tend to plot slightly above the bulk samples, confirming their higher glass content.

4.3. Main band and SiO_2 (Fig. 4c)

Another feature often easy to identify in remote sensing data is the broad MB of glassy materials. Comparison of the MB to the chemical composition in earlier studies (e.g., Morlok et al., 2020b) indicates a rather linear correlation at higher SiO_2 (>55 wt%). At lower contents, the trend line possibly splits – materials from vaporization experiments as proxy for hypervelocity impacts seem to continue the linear trends, while analog materials for melting and magmatic processes and synthetic basalts (Dufresne et al., 2009) indicate a horizontal trend, with lunar materials between the trends.

The lava analogs for Mercury in this study confirm and expand the horizontal trend for magmatic processes.

4.4. CF and crystallinity

The samples also provide an opportunity to test the influence of crystallinity on the CF. While the CF is often used as a proxy for the bulk composition, the influence of crystallinity should also be investigated.

The comparison of the average CF for all four size fractions of a given powdered sample with the modal abundance of melt or crystals indicates no significant correlation. At best a weak correlation is observed for the two larger size fractions, but the R^2 is at maximum 0.22, thus not significant. Looking only at grain size fractions 25 μm and larger to avoid potential influence of the different band shape of the finest fraction only slightly changes the correlation with a maximum R^2 of also 0.22. This shows that earlier observations (Nash and Salisbury, 1990; Weber et al., 2023) for crystalline and amorphous feldspars can also be extended to glass/crystalline mixtures in general with the same chemical bulk composition. However, it must be borne in mind that analysis of crushed and sieved materials may lead to a bias of phases in the different aliquots due to different mechanical properties of the minerals and due to the initial size of the phases. For example, the Moon's regolith is known to be enriched in feldspar in the finest fraction, and a similar behaviour can be expected on Mercury (Taylor et al., 2001; Reitze et al., 2021).

4.5. Comparison to Mercury remote sensing data (Fig. 5)

Remote sensing data for Mercury is difficult to obtain from ground-based observatories. Due to a long atmospheric column and closeness to the sun, useful spectra with high SNR are rare and cover large parts of the hermean surface (e.g. Sprague et al., 2007). For a comparison of our data with a hermean spectrum, we use a spectrum integrating the area between 210° and 250° longitude obtained by the Mid Infrared Camera (MIRAC) at the Kitt Peak Observatory (Sprague et al., 2000). The reflectance spectrum recalculated from emissivity using Kirchhoff's' law shows RB features at 9.2 μm, 9.9 μm, and 11 μm. The CF is at 8.5 μm, and the (potential) TF at 12.4 μm.

The CF is clearly shifted to shorter wavelength in all bulk and glass spectra in comparison to the surface spectrum. The crystalline components have CFs at longer wavelengths with up to 8.4 μm for enstatite in NVP, so a higher crystalline amount in the analog samples would shift the CF toward higher wavenumbers. For the RBs at 9.2 μm and 9.9 μm, enstatites from the bulk NVP samples (ID 406 and ID 413) would have features at comparable positions. Similar, crystalline micro-FTIR samples of ID 406 have also fitting bands for these two features on the hermean surface. However, none of the other strong features in these

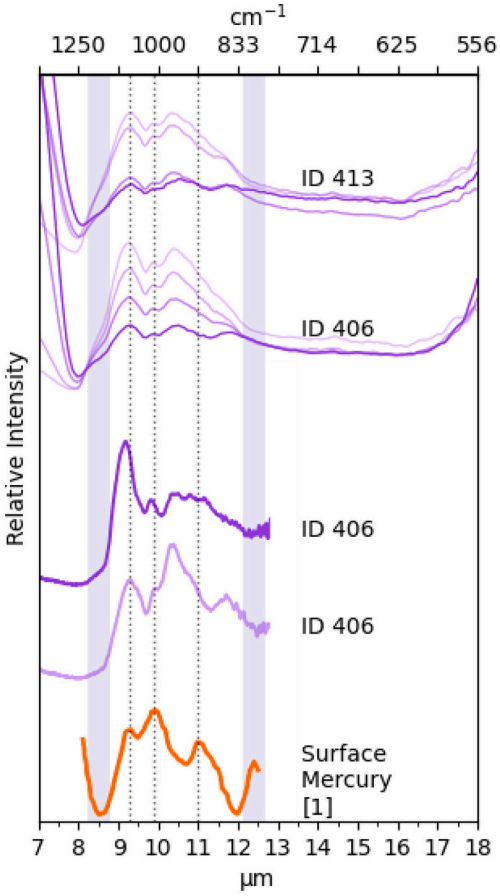

Fig. 5. Spectrum integrating hermean surface at 210°-250° longitude obtained by the Mid Infrared Camera (MIRAC) at the Kitt Peak Observatory ([1] = Sprague et al., 2000). The modelled reflectance has RB features at 9.2 µm, 9.9 µm and 11 µm. The CF is at 8.5 µm, and a potential TF at 12.4 µm. For comparison two bulk spectra from the NVP (ID 413 and ID 406), which show some similarity for the RBs at 9.2 µm and 9.9 µm. Two micro-FTIR spectra of enstatite from NVP ID 405 also indicate similar band positions at these positions.

NVP spectra are visible in the Mercury spectrum. The strong RB at 11 µm in the surface spectrum does not have equivalents in our analog spectra. The (potential) TF at 12.4 µm has some relatively close TF among the lava spectra with some TF at 12 µm.

However, the surface spectra are based on the integration of nearly half the hermean surface, so we expect a much more complex mineralogy with many other components, especially plagioclases. This probably requires a wider range of phases in modelling mixtures.

5. Conclusions

FTIR analyses of hermean lava analogs provided a series of characteristic spectra for enstatite basalt, the Northern Volcanic Plains, and Na-rich Northern Volcanic Plains.

Glass as the dominating phase forms a broad Si-O-Si stretching feature (Speck et al., 2011) around 10 µm. Crystalline components in the bulk studies are additional enstatite and forsterite with RBs around 9.3 µm, 9.6–9.9 µm, 10 µm, 10.3 µm - 10.7 µm.

These changes in the spectra reflect the constant increase in the content of crystallites in glass with decreasing temperature of equilibration and quenching (Fig. 2).

Micro-FTIR data allowed extraction of spectral data for distinct phases even in highly heterogeneous samples. Thus, spectra of 'pure' glass were extracted.

Correlation of spectral features to sample characteristics confirms correlations observed in earlier studies: the CF correlates well with the bulk SiO_2 content of the materials (Fig. 4a), as does the correlation of this feature with the polymerization index SCFM (Fig. 4b). The samples of this study also confirm the correlation line of glass-rich, irradiated and non-irradiated Mercury analogs (Weber et al., 2023). This indicates a similar spectral response of the glass-rich materials and analogue material is to be expected for the surface of Mercury.

When comparing the position of the strongest silicate feature (MB) to the SiO_2 content, the results cover an important compositional range of highly mafic materials and confirm trends indicated in earlier studies: the chemically similar material analogs for samples formed in high velocity impacts (Morlok et al., 2020b) fall on a different trend line than analog samples formed in magmatic processes (Fig. 4c).This has the potential to distinguish areas formed by magmatic processes from those resulting in hypervelocity impacts.

Furthermore, the samples allowed the investigation of the potential correlation/dependence of the CF to the degree of crystallinity, which was found to be very low and therefore confirmed earlier data by Nash and Salisbury (1990).

A preliminary comparison of the results to an Earth-based hermean surface spectrum showed similarities to spectra obtained for NVP samples, but no 'complete' fit. Further analog spectral studies are required.

However, when comparing and interpreting the results to remote sensing data, the impact of space environment on the data has to be kept in mind.

Systematic variation of pressure and temperature lunar environment conditions in studies of lunar regolith (Donaldson Hanna et al., 2017) showed that changing only pressure has the CF shifting to shorter wavelengths. An increase in temperature shifts the CF to longer wavelengths. Having both pressure and temperature under lunar conditions, the summary shift was up to 0.3 µm.

Temperature gradients under extreme vacuum and temperature conditions in the surface layers affect spectral contrast. This can distort band shapes and relative intensities and make detailed quantitative comparison difficult (Donaldson Hanna et al., 2017; Shirley and Glotch, 2019; Prem et al., 2022).

Porosity and grains size of the regolith also affect spectral features. Studies of asteroids (Emery et al., 2006; Vernazza et al., 2010, 2012) show that under low gravity a mixture of fine grained (<30 µm) and highly porous regolith forms 'fairy castle' structures. The resulting spectra are basically inverted, making comparison with laboratory data challenging.

Finally, space weathering plays a role in changing thin but spectroscopically important surface layers on airless bodies by producing glass and metallic iron (e.g. Weber et al., 2020, 2021, 2023; Stojic et al., 2021, 2023).

CRediT authorship contribution statement

Andreas Morlok: Writing – original draft, Visualization, Validation, Supervision, Software, Project administration, Methodology, Investigation, Conceptualization. **Alexander Sehlke:** Writing – review & editing, Resources, Methodology. **Aleksandra N. Stojic:** Writing – review & editing, Visualization, Investigation, Formal analysis. **Alan Whittington:** Writing – review & editing, Investigation, Conceptualization. **Iris Weber:** Writing – review & editing, Methodology, Investigation. **Maximilian P. Reitze:** Writing – review & editing, Investigation. **Harald Hiesinger:** Project administration, Funding acquisition. **Joern Helbert:** Funding acquisition.

Declaration of competing interest

The authors declare that they have no known competing financial interests or personal relationships that could have appeared to influence the work reported in this paper.

Data availability

The spectra presented in this study are available at the IRIS database of the Institut für Planetologie in Münster (http://bc-mertis-pl.uni-muenster.de).

Acknowledgements

AM, ANS, IW, MPR are supported by the DLR funding MERTIS FKZ 50QW2201A in the framework of the BepiColombo mission.

AS and AW are supported by NASA grant NNX12AO44G. AW is also supported by the NASA MIRO Center for Advanced Measurements in Extreme Environments, Grant 80NSSC19M019.

References

Allen, C.C., Greenhagen, B.T., Donaldson Hanna, K.L., Paige, D.A., 2012. Analysis of lunar pyroclastic deposit FeO abundances by LRO Diviner. J. Geophys. Res. Planets 117 (E12).

Charlier, B., Grove, T.L., Zuber, M.T., 2013. Phase equilibria of ultramafic compositions on Mercury and the origin of the compositional dichotomy. Earth Planet. Sci. Lett. 363, 50–60. https://doi.org/10.1016/j.epsl.2012.12.021.

Christensen, P.R., Bandlield, J.L, Hamilton, V.E., 2001. Mars global surveyor thermal emission spectrometer experiment: investigation description and surface science results. J. Geophys. Res. 106 (ElO), 23823–23872.

Cintala, M.J., 1992. Impact-induced thermal effects in the lunar and mercurian regoliths. J. Geophys. Res. Planets 97 (E1), 947–973.

Cooper, B., Potter, A., Killen, R., Morgan, T., 2001. Midinfrared spectra of mercury. J. Geophys. Res. 106, 32803–32814. https://doi.org/10.1029/2000JE001377.

Cooper, B.L., Salisbury, J.W., Killen, R.M., Potter, A.E., 2002. Midinfrared spectral features of rocks and their powders. J. Geophys. Res. (Planets) 107. https://doi.org/10.1029/2000JE001462. CiteID 5017.

Donaldson Hanna, K.L., Greenhagen, B.T., Patterson Iii, W.R., Pieters, C.M., Mustard, J. F., Bowles, N.E., Paige, D.A., Glotch, T.D., Thompson, C., 2017. Effects of varying environmental conditions on emissivity spectra of bulk lunar soils: application to Diviner thermal infrared observations of the Moon. Icarus 283, 326–342.

Dufresne, C.D.M., King, P.L., Dyar, M.D., Dalby, K.N., 2009. Effect of SiO2, total FeO, Fe3+/Fe2+, and alkali elements in basaltic glasses on mid-infrared spectra. Am. Mineral. 94, 1580–1590. https://doi.org/10.2138/am.2009.3113.

Emery, J.P., Cruikshank, D.P., Van Cleve, J., 2006. Thermal emission spectroscopy (5.2–38 μm) of three trojan asteroids with the spitzer space telescope: detection of fine-grained silicates. Icarus 182, 496–512. https://doi.org/10.1016/j.icarus.2006.01.011.

Emery, J.P., Sprague, A.L., Witteborn, F.C., Colwell, J.E., Kozlowski, R.W.H., Wooden, D. H., 1998. Mercury: thermal modeling and mid-infrared (5-12 μm) observations. Icarus 136, 104–123. https://doi.org/10.1006/icar.1998.6012.

Grard, R., Balogh, A., 2001. Returns to mercury: science and mission objectives. Planet. Space Sci. 49, 1395–1407. Returns to Mercury. https://doi.org/10.1016/S0032-0633(01)00081-2.

Hamilton, V.E., 2000. Thermal infrared emission spectroscopy of the pyroxene mineral series. J. Geophys. Res. 105, 9701–9716. https://doi.org/10.1029/1999JE001112.

Hamilton, V.E., 2010. Thermal infrared (vibrational) spectroscopy of Mg-Fe olivines: a review and applications to determining the composition of planetary surfaces. Chem. Erde – Geochem. 70, 7–33. https://doi.org/10.1016/j.chemer.2009.12.005.

Hapke, B., 1993. Theory of Reflectance and Emittance Spectroscopy. Cambridge Univ. Press, New York.

Harris, C.R., Millman, K.J., van der Walt, S.J., Gommers, R., Virtanen, P., Cournapeau, D., Wieser, E., Taylor, J., Berg, S., Smith, N.J., Kern, R., Picus, M., Hoyer, S., van Kerkwijk, M.H., Brett, M., Haldane, A., Fern, J., et al., 2020. Array programming with NumPy. Nature 585, 357–362. https://doi.org/10.1038/s41586-020-2649-2.

Hiesinger, H., Helbert, J., Mertis Co-I Team, 2010. The Mercury Radiometer and Thermal Infrared Spectrometer (MERTIS) for the BepiColombo mission. Planet. Space Sci. 58, 144–165. https://doi.org/10.1016/j.pss.2008.09.019.

Hiesinger, H., Helbert, J., Alemanno, G., Bauch, K.E., D'Amore, M., Maturilli, A., Morlok, A., Reitze, M.P., Stangarone, C., Stojic, A.N., Varatharajan, I., Weber, I., Mertis Co-I Team, 2020. Studying the composition and mineralogy of the Hermean surface with the Mercury Radiometer and Thermal Infrared Spectrometer (MERTIS) for the BepiColombo Mission: an update. Space Sci. Rev. 216 https://doi.org/10.1007/s11214-020-00732-4 article id.110.

Hofmeister, A.M., 1987. Single-crystal absorption and reflection infrared spectroscopy of forsterite and fayalite. Phys. Chem. Miner. 14, 499–513. https://doi.org/10.1007/BF00308285.

Hofmeister, A.M., 1997. Infrared reflectance spectra of fayalite, and absorption data from assorted olivines, including pressure and isotope effects. Phys. Chem. Miner. 24, 535–546. https://doi.org/10.1007/s002690050069.

Hunter, J.D., 2007. Matplotlib: a 2D graphics environment. Comp. Sci. Eng. 9, 90–95. https://doi.org/10.1109/MCSE.2007.55.

King, P.L., McMillan, P.F., Moore, G.M., 2004. Infrared spectroscopy of silicate glasses with application to natural systems. In: King, P.L., Ramsey, M.S., Swayze, G.A. (Eds.), Infrared Spectroscopy in Geochemistry, Exploration Geochemistry and Remote Sensing, Mineral. Assoc. Canada, Short Course Series, Vol. 33, pp. 93–133.

Lane, M.D., Glotch, T.D., Dyar, M.D., Pieters, C.M., Klima, R., Hiroi, T., Bishop, J.L., Sunshine, J., 2011. Midinfrared spectroscopy of synthetic olivines: thermal emission, specular and diffuse reflectance, and attenuated total reflectance studies of forsterite to fayalite. J. Geophys. Res. 116, E08010. https://doi.org/10.1029/2010JE003588.

Maturilli, A., Helbert, J., Moroz, L., 2008. The Berlin emissivity database (BED). Planet. Space Sci. 56, 420–425. https://doi.org/10.1016/j.pss.2007.11.015.

McCoy, T.J., Dickinson, T.L., Lofgren, G.E., 1999. Partial melting of the Indarch (EH4) Meteorite: a textural, chemical and phase relations view of melting and melt migration. Meteorit. Planet. Sci. 34, 735–746. https://doi.org/10.1111/j.1945-5100.1999.tb01386.x.

McKinney, W., 2010. Data structures for statistical computing in Python. In: Proceedings of the 9th Python in Science Conference, pp. 56–61.

Moersch, J.E., Christensen, P.R., 1995. Thermal emission from particulate surfaces: a comparison of scattering models with measured spectra. J. Geophys. Res. 100, 7465–7478. https://doi.org/10.1029/94JE03330.

Morlok, A., Stojic, A.N., Dittmar, I., Hiesinger, H., Tiedeken, M., Sohn, M., Weber, I., Helbert, J., 2016a. Mid-infrared spectroscopy of impactites from the Nördlinger Ries impact crater. Icarus 264, 352–368. https://doi.org/10.1016/j.icarus.2015.10.003.

Morlok, A., Stojic, A.N., Weber, I., Hiesinger, H., Zanetti, M., Helbert, J., 2016b. Mid-infrared bi-directional reflectance spectroscopy of impact melt glasses and tektites. Icarus 278, 162–179. https://doi.org/10.1016/j.icarus.2016.06.013.

Morlok, A., Bischoff, A., Patzek, M., Sohn, M., Hiesinger, H., 2017a. Chelyabinsk - a rock with many different (stony) faces: an infrared study. Icarus 284, 431–442. https://doi.org/10.1016/j.icarus.2016.11.030.

Morlok, A., Klemme, S., Weber, I., Stojic, A.N., Sohn, M., Hiesinger, H., 2017b. IR spectroscopy of synthetic glasses with Mercury surface composition: analogs for remote sensing. Icarus 296, 123–138. https://doi.org/10.1016/j.icarus.2017.05.024.

Morlok, A., Klemme, S., Weber, I., Stojic, A.N., Sohn, M., Hiesinger, H., Helbert, J., 2019. Mid-infrared spectroscopy of planetary analogs: a database for planetary remote sensing. Icarus 324, 86–103. https://doi.org/10.1016/j.icarus.2019.02.010.

Morlok, A., Weber, I., Stojic, A.N., Sohn, M., Bischoff, A., Martin, D., Hiesinger, H., Helbert, J., 2020a. Mid-infrared reflectance spectroscopy of aubrite components. Meteorit. Planet. Sci. 55, 2080–2096. https://doi.org/10.1111/maps.13568.

Morlok, A., Hamann, C., Martin, D., Weber, I., Joy, K.H., Hiesinger, H., Wogelius, R., Stojic, A.N., Helbert, J., 2020b. Mid-infrared spectroscopy of laser-produced basalt melts for remote sensing application. Icarus 335. https://doi.org/10.1016/j.icarus.2019.113410 article id. 113410.

Morlok, A., Renggli, C., Charlier, B., Reitze, M.P., Klemme, S., Namur, O., Sohn, M., Martin, D., Weber, I., Stojic, A.N., Hiesinger, H., Joy, K.H., Wogelius, R., Tollan, P., Carli, C., Bauch, K.E., Helbert, J., 2021. Mid-infrared reflectance spectroscopy of synthetic glass analogs for Mercury surface studies. Icarus 361. https://doi.org/10.1016/j.icarus.2021.114363 article id. 114363.

Morlok, A., Joy, K.H., Martin, D., Wogelius, R., Hiesinger, H., 2022. Laboratory IR spectroscopy of soils from Apollo 14, 15, and 16: spectral parameters and maturity. Planet. Space Sci. 223 https://doi.org/10.1016/j.pss.2022.105576 article id. 105576.

Morlok, A., Renggli, C., Charlier, B., Namur, O., Klemme, S., Reitze, M.P., Weber, I., Stojic, A.N., Bauch, K.E., Hiesinger, H., Helbert, J., 2023. A mid-infrared study of synthetic glass and crystal mixtures analog to the geochemical terranes on mercury. Icarus 396. https://doi.org/10.1016/j.icarus.2023.115498 article id. 115498.

Mustard, J.F., Hays, J.E., 1997. Effects of hyperfine particles on reflectance spectra from 0.3 to 25 μm. Icarus 125, 145–163. https://doi.org/10.1006/icar.1996.5583.

Namur, O., Charlier, B., 2017. Silicate mineralogy at the surface of Mercury. Nat. Geosci. 10, 9–13. https://doi.org/10.1038/ngeo2860.

Nash, D.B., Salisbury, J.W., 1990. Infrared reflectance spectra of plagioclase feldspars. Abstr. Lunar Planet. Sci. Conf. 21, #845.

Nicodemus, F.E., 1965. Directional reflectance and emissivity of an opaque surface. App. Optics IP 4 (767), 89. https://doi.org/10.1364/AO.4.000767.

Nittler, L.R., Starr, R.D., Weider, S.Z., McCoy, T.J., Boynton, W.V., Ebel, D.S., Ernst, C.M., Evans, L.G., Goldsten, J.O., Hamara, D.K., Lawrence, D.J., McNutt, R.L., Schlemm, C. E., Solomon, S.C., Sprague, A.L., 2011. The major-element composition of Mercury's surface from MESSENGER X-ray spectrometry. Science 333, 1847. https://doi.org/10.1126/science.1211567.

Nittler, L.R., Frank, E.A., Weider, S.Z., Crapster-Pregont, E., Vorburger, A., Starr, R.D., Solomon, S.C., 2020. Global major-element maps of Mercury from four years of MESSENGER X-ray spectrometer observations. Icarus 345. https://doi.org/10.1016/j.icarus.2020.113716 article id. 113716.

Peplowski, P.N., Stockstill-Cahill, K., 2019. Analytical identification and characterization of the major geochemical terranes of Mercury's northern hemisphere. J. Geophys. Res. Planets 124, 2414–2429. https://doi.org/10.1029/2019JE005997.

Peplowski, P.N., Lawrence, D.J., Feldman, W.C., Goldsten, J.O., Bazell, D., Evans, L.G., Head, J.W., Nittler, L.R., Solomon, S.C., Weider, S.Z., 2015. Geochemical terranes of Mercury's northern hemisphere as revealed by MESSENGER neutron measurements. Icarus 253, 346–363. https://doi.org/10.1016/j.icarus.2015.02.002.

Prem, P., Greenhagen, B.T., Donaldson Hanna, K.L., Shirley, K.A., Glotch, T.D., 2022. Modeling thermal emission under lunar surface environmental conditions. Planet. Sci. J. 3 https://doi.org/10.3847/PSJ/ac7ced id.180.

Reitze, M.P., Weber, I., Kroll, H., Morlok, A., Hiesinger, H., Helbert, J., 2020. Mid-infrared spectroscopy of alkali feldspar samples for space application. Mineral. Petrol. 114, 453–463. https://doi.org/10.1007/s00710-020-00709-9.

Reitze, M.P., Weber, I., Morlok, A., Hiesinger, H., Bauch, K.E., Stojic, A.N., Helbert, J., 2021. Mid-infrared spectroscopy of crystalline plagioclase feldspar samples with various Al, Si order and implications for remote sensing of Mercury and other

terrestrial Solar System objects. Earth Planet. Sci. Lett. 554 https://doi.org/10.1016/j.epsl.2020.116697 article id. 116697.
Reitze, M.P., Weber, I., Morlok, A., Hiesinger, H., Bauch, K.E., Stojic, A.N., Helbert, J., 2022. Mid-infrared spectroscopy of Anorthosite samples from near Manicouagan Crater, Canada, as analogue for remote sensing of Mercury and other terrestrial solar system objects. J. Geophys. Res. Planets 126. https://doi.org/10.1029/2021JE006832 article id. e06832.
Reitze, M.P., Weber, I., Morlok, A., Hiesinger, H., Pasckert, J.H., Schmedemann, N., Bauch, K.E., Stojic, A.N., Helbert, J., 2023. Mid-infrared spectroscopy of feldspars from the Bühl basalt (Northern Hesse, Germany) formed under reducing conditions as terrestrial analogue of Mercury for MERTIS. Earth Space Sci. 10 https://doi.org/10.1029/2023EA002903 article id. e2023EA002903.
Renggli, C.J., Klemme, S., Morlok, A., Berndt, J., Weber, I., Hiesinger, H., King, P.L., 2022. Sulfides and hollows formed on Mercury's surface by reactions with reducing S-rich gases. Earth Planet. Sci. Lett. 593 https://doi.org/10.1016/j.epsl.2022.117647 article id. 117647.
Rothery, D.A., Massironi, M., Alemanno, G., Barraud, O., Besse, S., Bott, N., Brunetto, R., Bunce, E., Byrne, P., Capaccioni, F., Capria, M.T., Carli, C., Charlier, B., Cornet, T., Cremonese, G., D'Amore, M., De Sanctis, M.C., Doressoundiram, A., Ferranti, L., Filacchione, G., Galluzzi, V., Giacomini, L., Grande, M., Guzzetta, L.G., Helbert, J., Heyner, D., Hiesinger, H., Hussmann, H., Hyodo, R., Kohout, T., Kozyrev, A., Litvak, M., Lucchetti, A., Malakhov, A., Malliband, C., Mancinelli, P., Martikainen, J., Martindale, A., Maturilli, A., et al., 2020. Rationale for BepiColombo studies of Mercury's surface and composition. Space Sci. Rev. 216 https://doi.org/10.1007/s11214-020-00694-7 article id.66.
Salisbury, J.W., Wald, A., 1992. The role of volume scattering in reducing spectral contrast of reststrahlen bands in spectra of powdered minerals. Icarus 96, 121–128. https://doi.org/10.1016/0019-1035(92)90009-V.
Salisbury, J.W., Walter, L.S., 1989. Thermal infrared (2.5-13.5 um) spectroscopic remote sensing of igneous rock types on particulate planetary surfaces. J. Geophys. Res. 94, 9192–9202. https://doi.org/10.1029/JB094iB07p09192.
Salisbury, J.W., Basu, A., Fischer, E.M., 1997. Thermal infrared spectra of lunar soils. Icarus 130 (1), 125–139.
Salisbury, J.W., D'Aria, D.M., Jarosewich, E., 1991. Midinfrared (2.5-13.5 μm) reflectance spectra of powdered stony meteorites. Icarus 92 (2), 280–297. https://doi.org/10.1016/0019-1035(91)90052-U.
Salisbury, J.W., Wald, A., D'Aria, D.M., 1994. Thermal-infrared remote sensing and Kirchhoff's law. 1. Laboratory measurements. J. Geophys. Res. 99, 11897–11911. https://doi.org/10.1029/93JB03600.
Schulz, R., Benkhoff, J., 2006. BepiColombo: payload and mission updates. Adv. Space Res. 38, 572–577. https://doi.org/10.1016/j.asr.2005.05.084.
Sehlke, A., Whittington, A.G., 2015. Rheology of lava flows on Mercury: an analog experimental study. J. Geophys. Res. Planets 120, 1924–1955. https://doi.org/10.1002/2015JE004792.
Shirley, K.A., Glotch, T.D., 2019. Particle size effects on mid-infrared spectra of lunar analog minerals in a simulated lunar environment. J. Geophys. Res. Planets 124, 970–988.
Speck, A.K., Whittington, A.G., Hofmeister, A.M., 2011. Disordered silicates in space: a study of laboratory spectra of 'amorphous' silicates. Astrophys. J. 740, 740. https://doi.org/10.1088/0004-637X/740/2/93.
Sprague, A.L., Roush, T.L., 1998. Comparison of laboratory emission spectra with Mercury telescopic data. Icarus 133, 174–183. https://doi.org/10.1006/icar.1998.5929.
Sprague, A.L., Kozlowski, R.W.H., Witteborn, F.C., Cruikshank, D.P., Wooden, D.H., 1994. Mercury: evidence for Anorthosite and basalt from mid-infrared (7.3-13.5 μm) spectroscopy. Icarus 109, 156–167. https://doi.org/10.1006/icar.1994.1083.
Sprague, A.L., Deutsch, L.K., Hora, J., Fazio, G.G., Ludwig, B., Emery, J., Hoffmann, W.F., 2000. Mid-infrared (8.1-12.5 μm) imaging of Mercury. Icarus 147, 421–432. https://doi.org/10.1006/icar.2000.6447.
Sprague, A.L., Emery, J.P., Donaldson, K.L., Russell, R.W., Lynch, D.K., Mazuk, A.L., 2002. Mercury: mid-infrared (3-13.5 μm) observations show heterogeneous composition, presence of intermediate and basic soil types, and pyroxene. Meteorit. Planet. Sci. 37, 1255–1268. https://doi.org/10.1111/j.1945-5100.2002.tb00894.x.
Sprague, A., Warell, J., Cremonese, G., Langevin, Y., Helbert, J., Wurz, P., Veselovsky, I., Orsini, S., Milillo, A., 2007. Mercury's surface composition and character as measured by ground-based observations. Space Sci. Rev. 132, 399–431. https://doi.org/10.1007/s11214-007-9221-3.
Stockstill-Cahill, K.R., McCoy, T.J., Nittler, L.R., Weider, S.Z., Hauck II, S.A., 2012. Magnesium-rich crustal compositions on Mercury: implications for magmatism from petrologic modeling. J. Geophys. Res. 117 https://doi.org/10.1029/2012JE004140. CiteID E00L15.
Stojic, A.N., Morlok, A., Tollan, P., Kohout, T., Hermann, J., Weber, I., Moreau, J.-G., Hiesinger, H., Sohn, M., Bauch, K.E., Reitze, M.P., Helbert, J., 2021. A shock recovery experiment and its implications for Mercury's surface: the effect of high pressure on porous olivine powder as a regolith analog. Icarus 357. https://doi.org/10.1016/j.icarus.2020.114162 article id. 114162.
Stojic, A.N., Weber, I., Morlok, A., Pavlov, S.G., Hiesinger, H., Reitze, M.P., Maturilli, A., Schmedemann, N., Bauch, K.E., Pasckert, J.H., Helbert, J., 2023. Simulation of surface regolith gardening and impact associated melt layer production under ns-pulsed laser ablation. Icarus 391. https://doi.org/10.1016/j.icarus.2022.115 article id. 115344.
Taylor, L.A., Pieters, C.M., Keller, L.P., Morris, R.V., McKay, D.S., 2001. Lunar mare soils: space weathering and the major effects of surface-correlated nanophase fe. J Geophys Res Planet 106, 27985–27999. https://doi.org/10.1029/2000JE001402 [R1-3].
Thomas, R.J., Rothery, D.A., Conway, S.J., Anand, M., 2015. Mechanisms of explosive volcanism on Mercury: implications from its global distribution and morphology. J. Geophys. Res. Planets 119, 2239–2254. https://doi.org/10.1002/2014JE004692.
Thomson, J.L., Salisbury, J.W., 1993. The mid-infrared reflectance of mineral mixtures (7-14 microns). Remote Sens. Environ. 45, 1–13. https://doi.org/10.1016/0034-4257(93)90077-B]344.
Vander Kaaden, K.E., McCubbin, F.M., 2016. The origin of boninites on Mercury: an experimental study of the northern volcanic plain's lavas. Geochim. Cosmochim. Acta 173, 246–263. https://doi.org/10.1016/j.gca.2015.10.016.
Vernazza, P., Carry, B., Emery, J., Hora, J.L., Cruikshank, D., Binzel, R.P., Jackson, J., Helbert, J., Maturilli, A., 2010. Mid-infrared spectral variability for compositionally similar asteroids: implications for asteroid particle size distributions. Icarus 207, 800–809. https://doi.org/10.1016/j.icarus.2010.01.011.
Vernazza, P., Delbo, M., King, P.L., Izawa, M.R.M., Olofsson, J., Lamy, P., Cipriani, F., Binzel, R.P., Marchis, F., Merín, B., Tamanai, A., 2012. High surface porosity as the origin of emissivity features in asteroid spectra. Icarus 221, 1162–1172.
Virtanen, P., Gommers, R., Oliphant, T.E., et al., 2020. SciPy 1.0: fundamental algorithms for scientific computing in Python. Nat. Methods 17, 261–272. https://doi.org/10.1038/s41592-019-0686-2.
Waskom, M.L., 2021. Seaborn: statistical data visualization. J. Open Source Softw. 6, 3021. https://doi.org/10.21105/joss.03021.
Weber, I., Morlok, A., Bischoff, A., Hiesinger, H., Ward, D., Joy, K.H., Crowther, S.A., Jastrzebski, N.D., Gilmour, J.D., Clay, P.L., Wogelius, R.A., Greenwood, R.C., Franchi, I.A., Münker, C., 2016. Cosmochemical and spectroscopic properties of Northwest Africa 7325—a consortium study. Meteorit. Planet. Sci. 51, 3–30. https://doi.org/10.1111/maps.12586.
Weber, I., Morlok, A., Grund, T., Bauch, K.E., Hiesinger, H., Stojic, A., Grumpe, A., Wöhler, C., Klemme, S., Sohn, M., Martin, D.J.P., Joy, K.H., 2018. A mid-infrared reflectance database in preparation for space missions. In: Lunar and Planetary Science Conference, Lunar and Planetary Science Conference. # 1430.
Weber, I., Stojic, A.N., Morlok, A., Reitze, M.P., Markus, K., Hiesinger, H., Pavlov, S.G., Wirth, R., Schreiber, A., Sohn, M., Hübers, H.-W., Helbert, J., 2020. Space weathering by simulated micrometeorite bombardment on natural olivine and pyroxene: a coordinated IR and TEM study. Earth Planet. Sci. Lett. 530 https://doi.org/10.1016/j.epsl.2019.115884 article id. 115884.
Weber, I., Reitze, M.P., Heeger, M., Adolphs, T., Morlok, A., Stojic, A.N., Hiesinger, H., Arlinghaus, H.F., Helbert, J., 2021. The effect of excimer laser irradiation on mid-IR spectra of mineral mixtures for remote sensing. Earth Planet. Sci. Lett. 569 https://doi.org/10.1016/j.epsl.2021.117072 article id. 117072.
Weber, I., Reitze, M.P., Morlok, A., Stojic, A.N., Hiesinger, H., Schmedemann, N., Bauch, K.E., Pasckert, J.H., Helbert, J., 2023. Mid-IR spectral properties of different surfaces of silicate mixtures before and after excimer laser irradiation. Icarus 404. https://doi.org/10.1016/j.icarus.2023.115683 article id. 115683.
Weider, S.Z., Nittler, L.R., Starr, R.D., Crapster-Pregont, E.J., Peplowski, P.N., Denevi, B. W., Head, J.W., Byrne, P.K., Hauck, S.A., Ebel, D.S., Solomon, S.C., 2015. Evidence for geochemical terranes on Mercury: global mapping of major elements with MESSENGER's X-Ray Spectrometer. Earth Planet. Sci. Lett. 416, 109–120. https://doi.org/10.1016/j.epsl.2015.01.023.
Williams, M.J., Schoneveld, L., Mao, Y., Klump, J., Gosses, J., Dalton, H., Bath, A., Barnes, S., 2020. Pyrolite: Python for geochemistry. J. Open Source Softw. 5, 2314. https://doi.org/10.21105/joss.02314.
Zeng, X., Li, X., Martin, D., Tang, H., Yu, W., Liu, J., Wang, S., 2019. Micro-FTIR Spectroscopy of Lunar Pyroclastic and Impact Glasses as a New Diagnostic Tool to Discern Them. J. Geophys. Res. Planets 124 (12), 3267–3282.